Flocking by Turning Away

Suchismita Das,[1] Matteo Ciarchi,[1] Ziqi Zhou,[2] Jing Yan,[3,4] Jie Zhang,[5,2,*] and Ricard Alert[1,6,7,†]

[1]*Max Planck Institute for the Physics of Complex Systems, Nöthnitzerstrasse 38, 01187 Dresden, Germany*
[2]*Department of Polymer Science and Engineering, University of Science and Technology of China (USTC), Hefei, Anhui 230026, China*
[3]*Department of Molecular, Cellular and Developmental Biology, Yale University, New Haven, Connecticut, USA*
[4]*Quantitative Biology Institute, Yale University, New Haven, Connecticut, USA*
[5]*Key Laboratory of Precision and Intelligent Chemistry, University of Science and Technology of China (USTC), Hefei, Anhui 230026, China*
[6]*Center for Systems Biology Dresden, Pfotenhauerstrasse 108, 01307 Dresden, Germany*
[7]*Cluster of Excellence Physics of Life, TU Dresden, 01062 Dresden, Germany*

(Received 16 February 2024; revised 8 May 2024; accepted 4 June 2024; published 12 July 2024)

Flocking, as paradigmatically exemplified by birds, is the coherent collective motion of active agents. As originally conceived, flocking emerges through alignment interactions between the agents. Here, we report that flocking can also emerge through interactions that turn agents away from each other. Combining simulations, kinetic theory, and experiments, we demonstrate this mechanism of flocking in self-propelled Janus colloids with stronger repulsion on the front than on the rear. The polar state is stable because particles achieve a compromise between turning away from left and right neighbors. Unlike for alignment interactions, the emergence of polar order from turn-away interactions requires particle repulsion. At high concentration, repulsion produces flocking Wigner crystals. Whereas repulsion often leads to motility-induced phase separation of active particles, here it combines with turn-away torques to produce flocking. Therefore, our findings bridge the classes of aligning and nonaligning active matter. Our results could help to reconcile the observations that cells can flock despite turning away from each other via contact inhibition of locomotion. Overall, our work shows that flocking is a very robust phenomenon that arises even when the orientational interactions would seem to prevent it.

DOI: 10.1103/PhysRevX.14.031008 Subject Areas: Soft Matter, Statistical Physics

I. INTRODUCTION

Flocking—the self-organized collective motion of active agents—is ubiquitous in nature [1]. It takes place in many systems across scales, from bird flocks [2] to bacterial colonies [3] and to cytoskeletal filaments driven by molecular motors [4]. Understood as the emergence of polar order in systems of self-propelled particles, flocking is a landmark phenomenon that launched the field of active matter [5,6]. As originally conceived in the Vicsek model [5], flocking arises through alignment interactions between the active agents, which align similarly to spins in the *XY* model. Alignment-based flocking has been experimentally realized using synthetic active colloids, which feature alignment interactions of either hydrodynamic, electric, or magnetic origin [7–9].

However, recent work showed that flocking can also emerge without explicit alignment interactions [10–13]. Instead of aligning with neighbors, the agents can experience a variety of alternative interactions [14–29], such as aligning with their own velocity or force [13–15], colliding inelastically [16,17], or chasing others in their vision cone [20–22].

Such alternative interactions were inferred in schooling fish [30,31], and they might be more widespread than standard alignment interactions. For example, robots in a swarm might benefit from collision-avoidance interactions that reorient them away from collisions [25,32]. Similarly, several types of motile cells undergo contact inhibition of locomotion—a behavior whereby cells repolarize away from cell-cell collisions [33–35]. Yet, cell layers and trains have been observed to flock, both in simulations [36,37] and in experiments [14,38–44]. How do cells flock despite interacting via contact inhibition of locomotion? More generally, what types of orientational interactions lead to flocking?

*Contact author: zhjie717@ustc.edu.cn
†Contact author: ralert@pks.mpg.de

Here, we show that agents that turn away from each other can collectively align and flock. This finding is surprising because turn-away interactions are intuitively expected to prevent and destroy orientational order. We show that this mechanism of flocking requires the combination of turn-away torques and repulsive forces between the particles. Therefore, our findings bridge the classes of alignment-based and repulsion-based phenomena in active matter, represented by flocking [45] and motility-induced phase separation [46], respectively. Our results expand the types of interactions that can produce flocking, and they might help to understand the physical origin of flocking in cell collectives. More generally, our results demonstrate the emergence of macroscopic polar order from microscopic interactions that do not implement polar alignment. Therefore, our findings strikingly showcase the disconnect between the symmetries of microscopic interactions and macroscopic order in active matter [23,47,48].

II. FLOCKING OF METAL-DIELECTRIC JANUS COLLOIDS

We study a suspension of self-propelled Janus colloidal particles [48–51]. The particles are 3-μm-diameter silica spheres, coated with 35 nm of titanium and 20 nm of silicon oxide on one hemisphere (Appendix A). These particles are suspended in deionized water and placed between conductive coverslips coated with indium tin oxide, separated by a 120 μm spacer [Fig. 1(a) and Appendix A]. Particles sediment to form a monolayer on the bottom coverslip. To drive the particles, we apply a perpendicular ac voltage of amplitude $V_0 = 10$ V and frequency $\nu = 30$ kHz. The resulting electric field aligns the particle equator perpendicular to the coverslips, and it polarizes the metal and dielectric hemispheres differently [Fig. 1(b)]. This difference induces (i) electrokinetic flows that produce particle self-propulsion along a direction $\hat{\boldsymbol{n}}$ pointing from the dielectric to the metallic hemisphere [52–54] and (ii) electrostatic interparticle forces and torques [Fig. 1(b)].

Upon application of the electric field, the system remains as an isotropic active gas at low area fractions and self-propulsion speeds [Fig. 1(c) and Movie 1 [55]]. In contrast, at higher area fractions and speeds, the system develops polar order and flocks [Fig. 1(d) and Movie 2 [55]]. In this regime, we observe spatiotemporal patterns including vortices and large-scale polar bands characteristic of flocking systems (Movies 3 and 4 [55]).

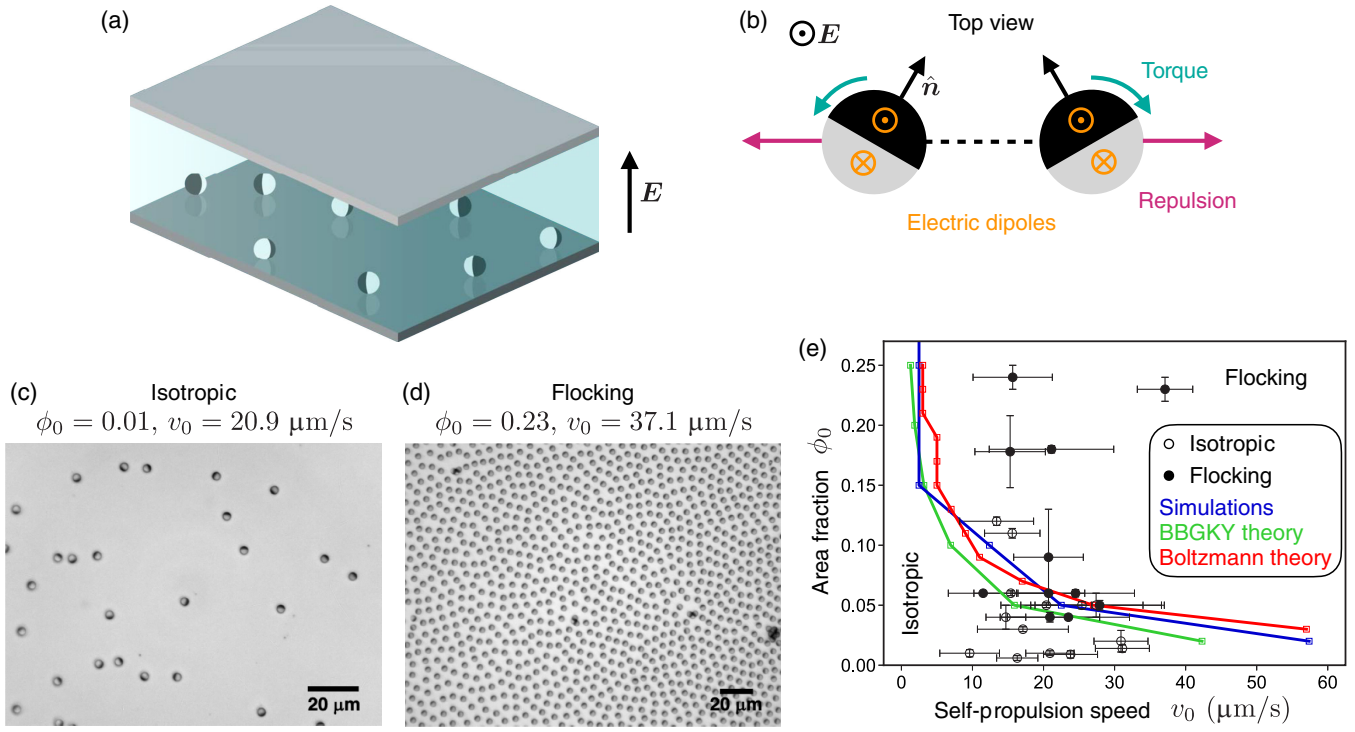

FIG. 1. Flocking of metal-dielectric Janus colloids. (a) Schematic of the experimental setup in which 3-μm-diameter particles are allowed to sediment in water to the bottom of a sample cell across which ac electric fields are applied vertically. (b) Top view of two Janus particles in an electric field $\boldsymbol{E}$ that induces dipoles of opposite orientation and different magnitude (orange) on the head and tail hemispheres. This leads to particle self-propulsion along the direction $\hat{\boldsymbol{n}}$ (black) and to interparticle forces (purple) and torques (green). Torques rotate particles away from the direction of the interparticle distance (dashed line). (c),(d) The system forms an isotropic gas at low area fraction and self-propulsion speed (c), and it flocks at high area fraction and speed (d). (e) Phase diagram of the flocking transition. Points show the experimental data. The lines indicate the phase boundaries that we predict via our simulations and two theory approaches. The experimental points are averages over time for durations ranging from 25 to 656 s, recorded at either 10 or 20 frames per second, including between 317 and 13 115 frames. Error bars are s.d.

We analyze different experimental realizations recorded at either high or low magnification. In high-magnification movies, we can track particle orientations $\hat{\boldsymbol{n}}_i(t)$ and measure the time-averaged polar order parameter $P = (1/N)\langle|\sum_{i=1}^{N}\hat{\boldsymbol{n}}_i(t)|\rangle_t$ (Figs. S1 and S2 [55]). In low-magnification movies, we cannot resolve single-particle orientations, and we instead perform particle image velocimetry to measure the flow field $\boldsymbol{v}(\boldsymbol{r})$ and obtain its correlation length (Figs. S3 and S4 [55]). Based on these measurements, we classify the state of each realization as either isotropic or flocking (Appendix A). Figure 1(e) shows that our experimental results are consistent with the simulations and theories that we develop below.

III. ACTIVE BROWNIAN PARTICLES WITH TURN-AWAY INTERACTIONS

The observation of flocking is surprising, as the electrostatic interactions between the particles tend to repel them and turn them away from each other [Fig. 1(b)]. To investigate if and how these interactions give rise to flocking, we use a two-dimensional microscopic model based on the dipolar interactions between the hemispheres of our particles [48]. Our model shows that two particles interact via a repulsive force

$$\boldsymbol{F}_{ij} = \frac{3}{4\pi\epsilon}\frac{(d_h + d_t)^2}{r_{ij}^4}e^{-r_{ij}/\lambda}\hat{\boldsymbol{r}}_{ij}, \tag{1}$$

where ϵ is the dielectric permittivity of the solvent, $\boldsymbol{r}_{ij} = \boldsymbol{r}_j - \boldsymbol{r}_i$ is the distance vector, and $d_h > 0$ and $d_t < 0$ are the effective dipole strengths of the head and tail hemispheres, respectively [Fig. 1(b)]. The exponential factor accounts for screening by the electrodes, separated by a distance $\lambda = 120$ μm. Moreover, because head dipoles are stronger than tail dipoles ($d_h^2 > d_t^2$), particles interact via a torque

$$\boldsymbol{\Gamma}_{ij} = \frac{3\ell}{4\pi\epsilon}\frac{d_h^2 - d_t^2}{r_{ij}^4}e^{-r_{ij}/\lambda}\hat{\boldsymbol{n}}_j \times \hat{\boldsymbol{r}}_{ij}, \tag{2}$$

where $\ell = 3R/8$ is the distance by which the dipoles are off-centered, with $R = 1.5$ μm the particle radius.

The torque in Eq. (2) tends to turn a particle with orientation $\hat{\boldsymbol{n}}_j$ away from the interparticle distance vector $\boldsymbol{r}_{ij}$ [Fig. 1(b)]. These turn-away interactions are fundamentally different from Vicsek-type alignment interactions: Whereas alignment interactions couple the orientations of two particles ($\boldsymbol{\Gamma}_{ij} \propto \hat{\boldsymbol{n}}_i \times \hat{\boldsymbol{n}}_j$), our turn-away interactions couple the orientation of one particle to the position of the other one ($\boldsymbol{\Gamma}_{ij} \propto \hat{\boldsymbol{n}}_j \times \boldsymbol{r}_{ij}$). As a result, turn-away torques are intrinsically nonreciprocal: $\boldsymbol{\Gamma}_{ij} \neq -\boldsymbol{\Gamma}_{ji}$.

We write Langevin equations for the translational and rotational motion of particle i as

$$\frac{d\boldsymbol{r}_i}{dt} = v_0\hat{\boldsymbol{n}}_i(\theta_i) + \frac{\boldsymbol{F}_i}{\xi_t} + \sqrt{2D_t}\boldsymbol{\eta}_i^t(t); \quad \boldsymbol{F}_i = \sum_{j\neq i}\boldsymbol{F}_{ji}, \tag{3a}$$

$$\frac{d\theta_i}{dt} = \frac{\Gamma_i}{\xi_r} + \sqrt{2D_r}\eta_i^r(t); \qquad \Gamma_i = \sum_{j\neq i}\boldsymbol{\Gamma}_{ji}\cdot\hat{\boldsymbol{z}}, \tag{3b}$$

where v_0 is the self-propulsion speed, $\hat{\boldsymbol{n}}_i = (\cos\theta_i, \sin\theta_i)$ is the orientation of particle i, ξ_t and ξ_r are the translational and rotational friction coefficients, respectively, and $\boldsymbol{\eta}_i^t(t)$ and $\eta_i^r(t)$ are Gaussian white noises with strengths given by the translational and rotational diffusivities D_t and D_r, respectively. We perform Brownian dynamics simulations of this model with N particles in a square box of side L with periodic boundary conditions (Appendix A and parameter values in Table I). We benchmark the simulations by reproducing the phase separation reported in Ref. [48], which is induced by torques that turn particles toward one another, with $d_t^2 > d_h^2$ (Fig. S5 [55]).

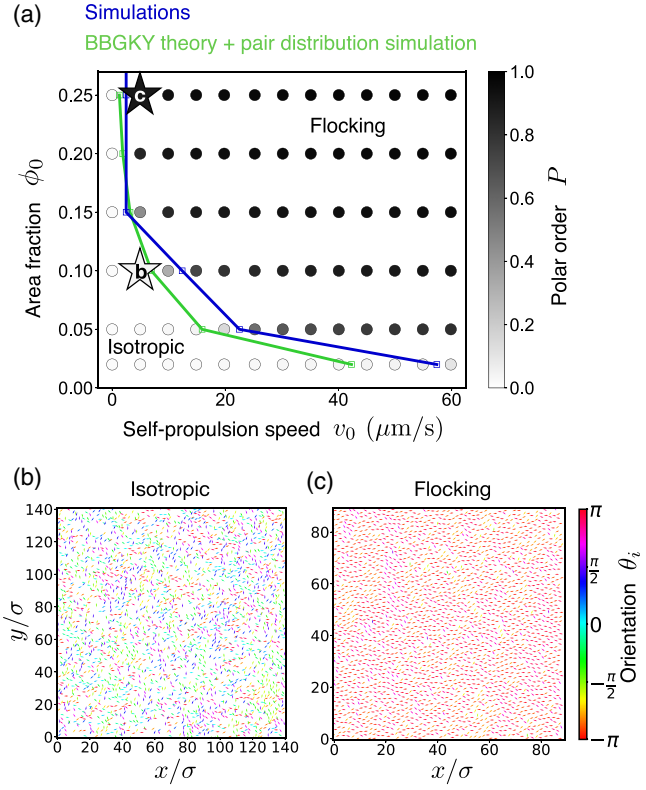

FIG. 2. Flocking in simulations of repulsive active Brownian particles with turn-away torques. (a) Phase diagram showing the flocking transition as either the area fraction or the self-propulsion speed increases. The blue phase boundary is obtained from the point of steepest ascent of the measured polar order parameter P (Fig. S7 [55]). The green phase boundary is predicted using BBGKY kinetic theory using the pair distribution function measured in simulations [Figs. 4(b)–4(e)]. Stars indicate the snapshots shown below. (b),(c) Snapshots showing the isotropic phase (b) and the polar flocking phase (c). The evolution toward the flocking state is shown in Fig. S8 and Movie 6 [55].

For turn-away torques, with $d_h^2 > d_t^2$, our simulations with $N = 2500$ show the emergence of global polar order P as we increase either the self-propulsion speed v_0 or the global area fraction $\phi_0 = N\pi R^2/L^2$ (Fig. 2 and Movies 5 and 6 [55]). Global polar order also emerges in larger simulations of up to $N = 70\,225$ (Fig. S6 [55]), suggesting that the flocking transition survives in the large-system limit. We conclude that active Brownian particles can flock despite turning away from one another. Moreover, the phase boundary obtained from simulations [Fig. 2(a), blue line] is quantitatively close to the transition that we observe in experiments [Fig. 1(e)].

IV. ACTIVE WIGNER CRYSTALS

As we increase the area fraction in simulations beyond those in our experiments, flocks develop crystalline order (Fig. 3). These states are reminiscent of flocking crystals reported in previous simulations [56,57]. However, whereas ordinary crystals form by attraction between the particles, the force in our model is purely repulsive [Eq. (1)]. Thus, the flocking crystals that we find are active counterparts of Wigner crystals, which were originally proposed to form through electrostatic repulsion in electron gases [58]. In our system, the repulsion includes both the electrostatic repulsive force in Eq. (1) as well as an effective repulsion arising from the turn-away torques in Eq. (2) and self-propulsion [36,59]. Therefore, turn-away torques promote the formation of active Wigner crystals.

In two dimensions, crystallization involves an intermediate hexatic phase with orientational order in the particle positions [60]. We obtain the global hexatic order parameter ψ_6, which goes from 0 in the liquid phase to 1 for a monodomain triangular lattice [Fig. 3(a) and Appendix A]. We then use orientational and positional correlations to identify the transitions to the hexatic and crystalline phases (Fig. S9 [55]), marked with dashed lines in Fig. 3(a). Consistently with previous works [61,62], increasing activity v_0 in the crystalline phase [Figs. 3(d) and 3(e)] promotes the formation of a single crystal spanning the entire system. The polycrystalline states at low activity v_0 [Fig. 3(d)] last for the entire duration of our simulations.

Although they both depend on the turn-away torques, the flocking and the crystallization transitions remain separate. Below the crystallization threshold, we observe fluid flocks [Figs. 3(a) and 3(b)]. Crystallization is, therefore, not required for flocking via turn-away torques. In fact, as we increase the area fraction in larger systems with $N = 40\,000$ particles, we observe flocks in the form of well-known polar bands and uniform liquids [7,12,45] before reaching hexatic states and active Wigner crystals (Fig. S10 and Movies 7–11 [55]). Overall, crystallization is not involved in the mechanism whereby particles with turn-away interactions flock.

V. COARSE-GRAINING SHOWS THAT CORRELATIONS ENABLE FLOCKING

To understand the emergence of polar order, we coarse-grain the microscopic model [Eq. (3)]. To this end, we write the Smoluchowski equation and break it into the Bogoliubov-Born-Green-Kirkwood-Yvon (BBGKY) hierarchy to obtain an equation for the one-particle distribution function, from which we obtain hydrodynamic equations

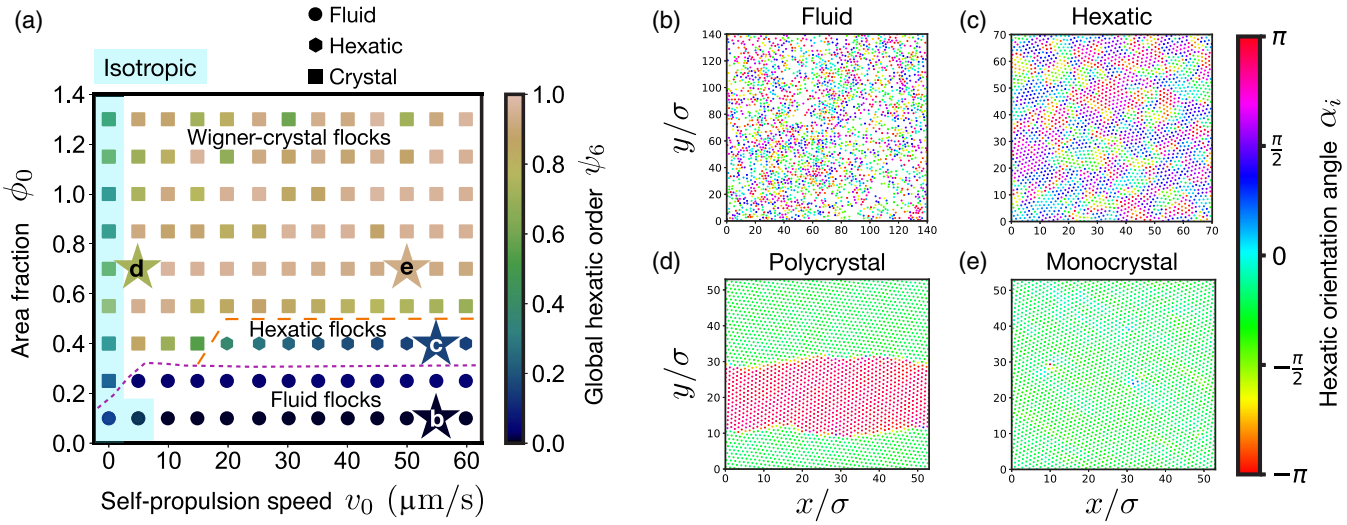

FIG. 3. Active Wigner crystals. (a) At high area fraction, the system forms flocking Wigner crystals, which have high values of the global hexatic order parameter ψ_6. The hexatic and crystalline phases are identified from orientational and positional correlations (Fig. S9 [55]), and phase boundaries (dashed lines) are guides to the eye. Stars indicate the snapshots shown in the other panels. (b)–(e) Snapshots of fluid, hexatic, and crystalline flocks. Crystals are typically polycrystalline with grain boundaries at low activity (d) and monocrystalline at higher activity (e). Color indicates the angle α_i between the local hexatic order of each particle and its average over the system (Appendix A).

for the density and the polarity fields $\rho(\boldsymbol{r},t)$ and $\boldsymbol{P}(\boldsymbol{r},t)$ (Appendix B). For the polarity, we obtain

$$\partial_t \boldsymbol{P} = a[\rho]\boldsymbol{P} + \mathcal{O}(\boldsymbol{\nabla}). \tag{4}$$

Polar order emerges if $a > 0$. The coarse-graining yields

$$a[\rho] = \frac{\rho}{2\pi\xi_r}\tau_0 - D_r, \tag{5}$$

where the first term is due to torques and the second term represents the decay of polar order due to rotational diffusion. The effect of the torques, expressing Eq. (2) as $\boldsymbol{\Gamma}_{ij} = \Gamma(r)\hat{\boldsymbol{n}}_j \times \hat{\boldsymbol{r}}_{ij}$ with $r = |\boldsymbol{r}_{ij}|$, is embodied in the coefficient τ_0, which is given by (Appendix B)

$$\tau_0 = \int_0^\infty r dr \int_0^{2\pi} d\varphi \int_0^{2\pi} d\theta \sin\theta \Gamma(r) \sin\varphi g(r,\varphi,\theta) \tag{6}$$

in terms of the pair distribution function $g(r,\varphi,\theta)$ in the isotropic state [23]. This function encodes correlations, as it gives the probability density of finding a pair of particles at a distance r, with the second particle at a position and orientation forming angles φ and θ with respect to the orientation of the reference particle: $\hat{\boldsymbol{n}}_i \cdot \hat{\boldsymbol{r}}_{ij} = \cos\varphi$ and $\hat{\boldsymbol{n}}_i \cdot \hat{\boldsymbol{n}}_j = \cos\theta$ [Fig. 4(a)].

Which properties must the pair distribution g have in order to yield a nonzero τ_0 that could produce flocking? To prevent the angular integrals in Eq. (6) from vanishing by symmetry [63], g has to fulfill the following conditions:

(i) $g(r,-\varphi,\theta) \neq g(r,\varphi,\theta)$,
(ii) $g(r,\varphi,-\theta) \neq g(r,\varphi,\theta)$,
(iii) $g(r,\varphi+\pi,\theta) \neq g(r,\varphi,\theta)$, and
(iv) $g(r,\varphi,\theta+\pi) \neq g(r,\varphi,\theta)$.

These conditions are necessary, but not sufficient, for flocking.

To test whether these conditions are satisfied, we measure $g(r,\varphi,\theta)$ in our simulations (Appendix A). As g is a function of three arguments, we plot $g(r,\varphi)$ and bin the relative orientations in the four quadrants of the angle θ [Figs. 4(b)–4(e)]. These plots show a clear asymmetry upon changing the sign of the polar angle $\varphi \to -\varphi$. There is also a clear asymmetry upon the transformation $\theta \to -\theta$, which corresponds to exchanging the first quadrant with the fourth [Figs. 4(b) and 4(e)] and the second with the third [Figs. 4(c) and 4(d)]. Therefore, our system satisfies conditions (i) and (ii). Furthermore, for a given quadrant of θ, changing $\varphi \to \varphi + \pi$ corresponds to moving to the diametrically opposed point, which yields a different value of g. Respectively, changing $\theta \to \theta + \pi$ corresponds to exchanging the first quadrant with the third [Figs. 4(b) and 4(d)] and the second with the fourth [Figs. 4(c) and 4(e)], which again yields different values of g. Therefore, our system also satisfies conditions (iii) and (iv).

These results show that the correlations in our system fulfil the necessary requirements to yield flocking. We then use the measured pair distribution to predict the flocking transition. To this end, we introduce the measured $g(r,\varphi,\theta)$ into Eq. (6) to obtain the growth rate a of polar order in Eq. (5) for different values of the area fraction ϕ_0 and self-propulsion speed v_0 [Fig. 4(f)]. The change of sign of a marks the predicted onset of flocking, shown as the green line in Figs. 1(e) and 2(a), which agrees quite well with the experimental results [Fig. 1(e)]. Our theory, therefore, captures the flocking transition.

Once polar order has emerged, turn-away torques stabilize it. In contrast to alignment interactions, turn-away interactions hinder the formation of polar clusters, as particles at the cluster edge turn away and move into low-density areas. Therefore, turn-away interactions produce flocking states in which particles always have lateral neighbors. As a result, if a particle deviates from the flocking direction, it moves closer to a neighbor and experiences a torque that restores its initial orientation [Fig. 4(g)]. Flocking, therefore, represents a compromise between turning away from left and right neighbors.

VI. FLOCKING EMERGES FROM TURN-AWAY TORQUES AND REPULSION

Our findings so far indicate that, already in the isotropic state, the system builds up correlations that enable the emergence of polar order. Where do these correlations come from? We argue that they arise from the combined effects of turn-away torques and repulsion forces. Taking Fig. 4(b) as an example, the peaks of g are found in regions of low turn-away torque [as shown in Fig. 4(h)], where particles tend to stay longer. In other quadrants, these low-torque regions change precisely in the way required to satisfy conditions (i) and (ii) (Fig. S11 [55]). Respectively, the asymmetry between the front and the back peaks in Fig. 4(b), required for condition (iii), is due to repulsion. Whereas particles at the front are pushed forward and sped up by repulsion, particles at the back are pushed back and slowed down [Fig. 4(i)], which makes them stay longer. Finally, condition (iv) is satisfied due to the difference in relative velocity between the particles: The correlations when two particles move in the same direction are different than when they move in opposite directions. We conclude that, together, turn-away torques and repulsion provide the conditions for flocking.

VII. BOLTZMANN KINETIC THEORY PREDICTS EFFECTIVE ALIGNMENT

To gain microscopic insight into how torques and repulsion jointly produce flocking, we analyze binary scattering events. We choose the axes so that the two particles are separated along the $\hat{\boldsymbol{y}}$ axis [Fig. S12(a) [55]]. Then, a scattering event between particles with orientations θ_1 and θ_2 is characterized by the incoming half-angle $\bar{\theta} = \arg(e^{i\theta_1} + e^{i\theta_2})$ and the angle difference $\theta = \theta_2 - \theta_1$ [Fig. S12(b) [55]]. We first consider an event with $\bar{\theta} = 0$,

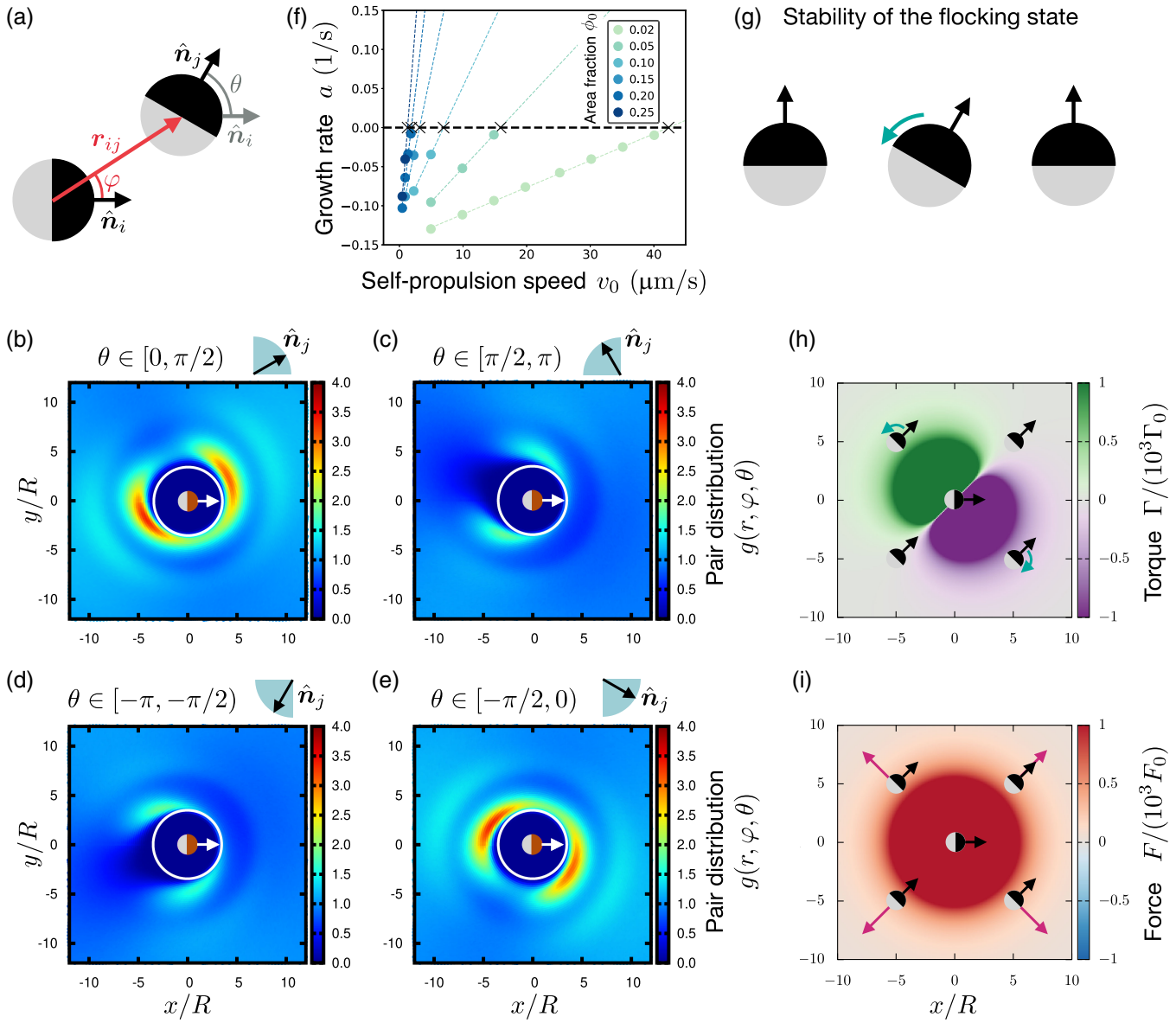

FIG. 4. Correlations established by turn-away torques and repulsion enable the emergence of polar order. (a) Definitions of the arguments r, φ, and θ of the pair distribution function. (b)–(e) Pair distribution function measured in simulations in the isotropic state, for $\phi_0 = 0.1$ and $v_0 = 5$ μm/s, built as histograms over 1000 independent configurations. The four panels show $g(r, \varphi)$ for particle pairs with relative orientation θ in each of the four quadrants, as indicated. The white circumferences around the reference particle indicate the predicted exclusion region, which we obtain as the distance r^* at which repulsion overcomes the self-propulsion force: $F(r^*) = \xi_t v_0$, with Eq. (1) expressed as $\boldsymbol{F}_{ij} = F(r)\hat{\boldsymbol{r}}_{ij}$. (f) Growth rate calculated using Eq. (5) with Eq. (6) using the $g(r, \varphi, \theta)$ measured in simulations. The black crosses, obtained by extrapolation, indicate the onset of flocking, which determines the green phase boundary in Fig. 2(a). (g) Schematic showing that torques stabilize the flocking state: Turning away from both the left and right neighbors keeps particles moving together. (h), (i) Torque and force fields, respectively, exerted by the reference particle on a particle with relative orientation $\theta = \pi/4$, as indicated. This orientation belongs to the first quadrant (b). Green arrows in (h) and purple arrows in (i), respectively, indicate the directions of the torque and repulsive force on each of the probe particles, which explain the pair distribution in (b). The torque and force are plotted from Eq. (1) and (1) and normalized by $\Gamma_0 = 3\ell(d_h^2 - d_t^2)/(4\pi\epsilon R^4)$ and $F_0 = 3(d_h + d_t)^2/(4\pi\epsilon R^4)$.

and we analyze scattering with torques only [Fig. 5(a)]. If particles come into the interaction range r_{int} at an angle difference θ_{in}, they turn away from each other and they exit the interaction range with angle difference $\theta_{\text{out}} = -\theta_{\text{in}}$ [Fig. 5(a)]. The momentum of the pair does not change. Therefore, turn-away torques alone do not yield any alignment during this scattering event.

Repulsion, however, pushes particles out of the interaction range before they have time to turn completely [Fig. 5(b)]. Therefore, particles leave the scattering event

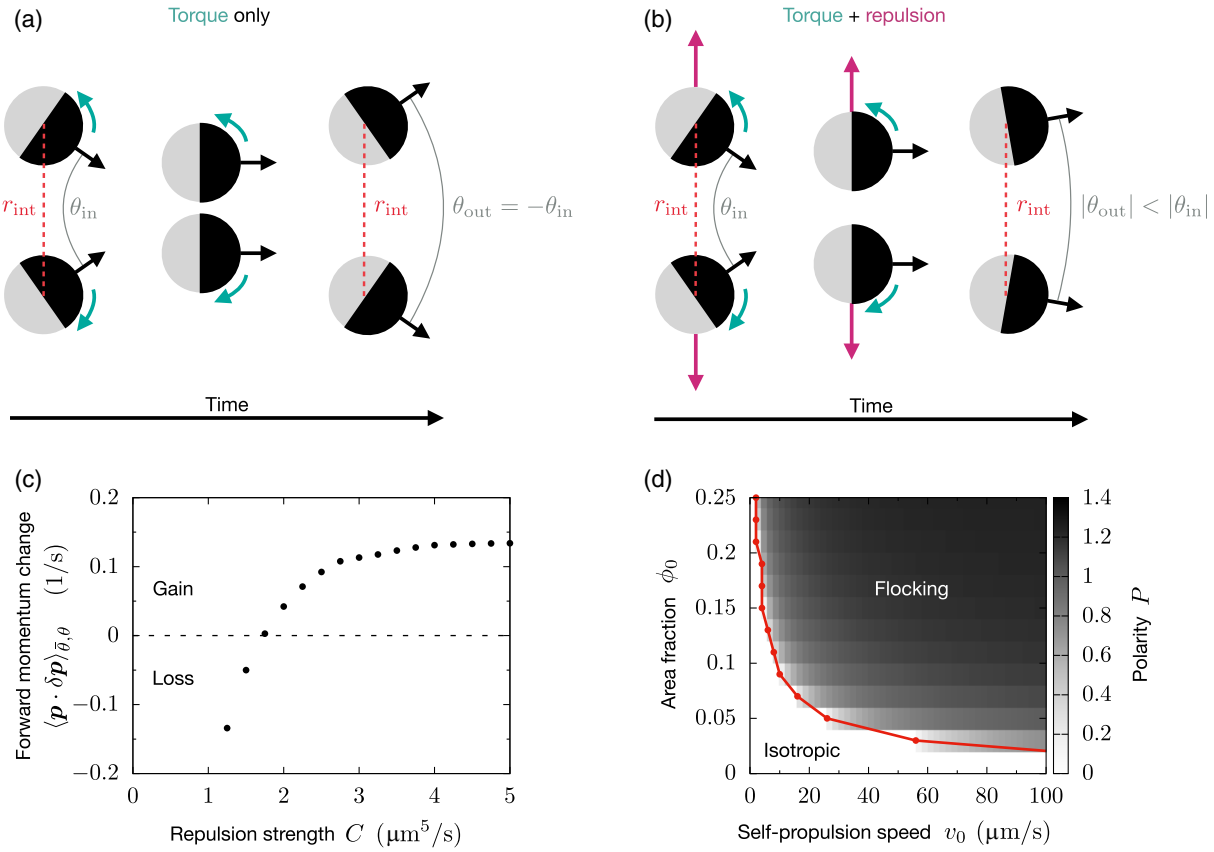

FIG. 5. Repulsion and turn-away torques produce effective alignment during scattering events. (a),(b) Schematics of a symmetric scattering event, for which turn-away torques alone do not yield any alignment (a) whereas adding repulsion does (b). (c) Scattering events produce a gain in forward momentum [Eq. (7)] only in the presence of enough repulsion. The repulsion strength C is defined from Eq. (1) by $F(r) = Ce^{-r/\lambda}/r^4$ [see Eq. (A1) in Appendix A]. (d) Phase diagram of flocking predicted from the Boltzmann kinetic theory [Eq. (7) and Appendix C]. The phase boundary is marked in red. The polarity P is obtained from Eq. (A4) (see Appendix A).

with a smaller angle difference than initially: $|\theta_{\rm out}| < |\theta_{\rm in}|$. The combined effects of turn-away torques and repulsion, therefore, cause effective alignment, and, hence, they can produce flocking.

To average over scattering events, we use Boltzmann's kinetic theory generalized for self-propelled particles [64]. This theory predicts that the growth rate of polar order, as in Eq. (4), is given by $a = \langle \boldsymbol{p} \cdot \delta\boldsymbol{p} \rangle_{\bar\theta,\theta} - D_r$, where the first term is the average over scattering events of the dimensionless momentum change $\delta\boldsymbol{p}$ in the forward direction, i.e., projected on the incoming momentum $\boldsymbol{p} = \hat{\boldsymbol{n}}_1 + \hat{\boldsymbol{n}}_2$. In our case, it is given by (Appendix C)

$$\langle \boldsymbol{p} \cdot \delta\boldsymbol{p} \rangle_{\bar\theta,\theta} = \frac{\rho v_0 r_{\rm int}}{2\pi} \int_{-\pi}^{\pi} d\theta |\sin(\theta/2)| \langle \boldsymbol{p} \cdot \delta\boldsymbol{p}(\bar\theta,\theta) \rangle_{\bar\theta}, \quad (7)$$

where $r_{\rm int} = \lambda$ is the interaction range. This forward momentum change quantifies the effective alignment arising from scattering events. To obtain it, we numerically integrate the equations of motion Eq. (3) without noise for binary scattering events with different $\bar\theta$ (Appendix A). The results show that having forward momentum gain requires repulsion [Fig. 5(c)], which is, therefore, necessary for flocking. Finally, we use the scattering statistics to predict the growth rate a and, hence, the onset of flocking for $a = 0$ [Fig. 5(d), red line]. These predictions, which include only two-particle dynamics, are consistent with our many-particle simulation results and with our experiments [Fig. 1(e)]. Together, these results reveal the microscopic mechanism responsible for flocking through combined repulsion and turn-away torques.

VIII. DISCUSSION AND OUTLOOK

In summary, we discovered a mechanism that allows self-propelled particles to flock by repelling and turning away from each other. This finding sharply contrasts with the mechanism of flocking in the paradigmatic Vicsek model, which relies on explicit alignment interactions between the active agents. In that case, flocking emerges purely from torques; it does not require any central forces between the agents. In contrast, we revealed a mechanism of flocking that relies on both torques and repulsion, thus combining features of aligning and nonaligning active matter.

Recent work reported that flocking can arise from collision-avoidance interactions, which align particles by turning them

away from a collision [23,25]. Our turn-away interactions, however, can produce severe misalignment, as particles keep turning away from each other even after they have avoided collision, thus making flocking seemingly impossible. Our results show that flocking emerges even in this case.

At high densities and speeds, alignment-based flocks made of Quincke rollers were previously found to lose polar order as they experience motility-induced phase separation (MIPS) [65]. However, the turn-away torques in our system hinder MIPS, as they reorient particles away from clusters [24]. Therefore, flocks obtained through turn-away interactions can achieve higher speeds and densities without suffering phase separation and loss of collective motion. This feature allows us to obtain flocks in the form of dense liquids and Wigner crystals produced by particle repulsion. Similar crystals, albeit without flocking, were obtained recently in simulations of microswimmers with chemorepulsive interactions [66].

Active particles often crystallize via either MIPS [50,67–69] or hydrodynamic attraction [70–73] or by approaching close packing [74–76], all of which produce particle collisions and impair collective motion. Here, Wigner crystallization keeps particles at a distance, which avoids collisions and does not impair collective motion.

As an outlook, we speculate that flocking by turning away might contribute to collective motion in cell populations, possibly solving the apparent paradox that cells can flock despite interacting via contact inhibition of locomotion [36,37,77]. Interactions between cells are much more complex than those between our active colloids. Yet, as mesenchymal cells repolarize away from each other upon collision, cell-cell scattering events could have outcomes similar to those between our particles, with an outgoing angle larger than zero but smaller in magnitude than the incoming angle [Fig. 5(b)]. We look forward to experimental tests of this idea in future work.

Finally, flocking by turning away might also provide a strategy to engineer robust swarming in disordered environments. We already saw hints of this robustness in our experiments, in which flocks easily flow past stuck particles (Movies 2 and 4 [55]). If an agent gets stuck at an obstacle, alignment interactions will produce accumulation of followers behind it. Instead, turn-away interactions allow followers to readily reorient away, which might yield smoother and more efficient flocking through disordered landscapes.

ACKNOWLEDGMENTS

We thank Jonathan Bauermann, Fridtjof Brauns, Kartik Chhajed, Erwin Frey, Steve Granick, Robert Großman, Frank Jülicher, Debasmit Sarkar, Jeanine Shea, Holger Stark, John Toner, and Till Welker for discussions. We thank Mariona Esquerda Ciutat for Fig. 1(a). We acknowledge computing support by the Max Planck Computing and Data Facility and the computing facility at MPI-PKS. Z. Z. and J. Z. acknowledge financial support from the National Natural Science Foundation of China (NSFC) (Grant No. 12204453) and University of Science and Technology of China (YD2060002028, WK3450000008, and KY2060000211). Z. Z. and J. Z. acknowledge the Supercomputing Center of University of Science and Technology of China (USTC) for proving computational resources. The experimental work was partially carried out at the Center for Micro and Nanoscale Research and Fabrication and the Instruments Center for Physical Science, University of Science and Technology of China.

S. D. performed and analyzed the Brownian dynamics simulations. S. D. and R. A. developed the BBGKY hierarchy calculations. M. C. performed the scattering calculations and simulations. J. Y. performed the initial set of experiments during his Ph.D. J. Z. performed additional experiments. S. D., Z. Z., J. Y., and J. Z. analyzed the experimental data. R. A. conceived and supervised the work. S. D., M. C., and R. A. wrote the paper.

APPENDIX A: METHODS

1. Particle synthesis

Following protocols described elsewhere [49], a submonolayer of 3-μm-diameter silica particles (Tokuyama) is prepared on a standard glass slide. Then, 35 nm of titanium and then 20 nm of SiO_2 are deposited vertically on the glass slide using an electron-beam evaporator. The preparation is then washed with isopropyl alcohol and deionized water and then sonicated into deionized water to collect the Janus particles.

2. Experimental setup

The particle suspensions are confined between two coverslips (SPI Supplies) coated with indium tin oxide to make them conductive and with 25 nm of silicon oxide to prevent particles from sticking to them. The coverslips have a 9 mm hole in the center, separated by a 120-μm-thick spacer (GraceBio SecureSeal), where we place the suspension of Janus colloidal particles. An alternating voltage is applied between the coverslips using a function generator (Agilent 33522A). The sample cell is imaged with 5×, 40×, and 64× air objectives on an inverted microscope (Axiovert 200). The observation areas are 1232 μm × 1640 μm, 154 μm × 205 μm, and 96 μm × 128 μm, respectively. Microscopic images and videos are taken with a CMOS camera (Edmund Optics 5012M GigE) with 20 ms time resolution.

3. Image analysis

Image processing is performed using MATLAB with home-developed codes.

4. Experimental data analysis

Here, we describe the analysis methods that we use to identify flocking in the experimental movies. We analyze experimental movies obtained with three different magnifications: 64×, 40×, and 5×.

For 64× and 40× magnifications, we can track particle orientations $\hat{\boldsymbol{n}}_i(t)$ and obtain the polar order parameter $P(t) = (1/N)|\sum_{i=1}^{N} \hat{\boldsymbol{n}}_i(t)|$ (Fig. S1 [55]). We classify as flocking the experimental realizations for which the time-averaged polar order parameter is $\langle P(t)\rangle_t \geq 0.5$.

For 5× magnification, we cannot resolve single-particle orientations $\hat{\boldsymbol{n}}_i(t)$, and, hence, we can study polar order only indirectly through the flow field $\boldsymbol{v}(\boldsymbol{r}, t)$, which we measure using particle image velocimetry. Analyzing high-magnification videos, we find that the polar order parameter obtained from particle orientations, $P_n(t) = P(t) = (1/N)|\sum_{i=1}^{N} \hat{\boldsymbol{n}}_i(t)|$, strongly correlates with that obtained from the particle velocity axes $\hat{\boldsymbol{v}}_i(t)$ as $P_v(t) = (1/N)|\sum_{i=1}^{N} \hat{\boldsymbol{v}}_i(t)|$ (Fig. S2 [55]). Hence, the velocity field approximates well the polarity field, and we, therefore, use it to characterize polar order in low-magnification movies.

To do this, we obtain the spatial correlation function of the velocity field, $C(r, t) = \langle \boldsymbol{v}(r, t) \cdot \boldsymbol{v}(0, t)\rangle$. We then fit to it an exponential decay $C(r, t) \sim e^{-r/\xi(t)}$, from which we extract the velocity correlation length $\xi(t)$ (Fig. S3 [55]). We expect flocking states to have a correlation length substantially larger than the average interparticle distance $\langle r\rangle = \sqrt{1/\rho} = R\sqrt{\pi/\phi_0}$. We classify as flocking the experimental realizations for which the time-averaged correlation length is larger than 10 times the average interparticle distance: $\langle \xi(t)\rangle_t \geq 10\langle r\rangle_{\boldsymbol{r},t}$ (Fig. S4 [55]). This threshold seems to be a good compromise between requiring relatively long-ranged correlations and accounting for the finite size of the polar domains throughout our experiments. In most movies that visually exhibit some polar order, the polar domains are not much bigger than this threshold size. Therefore, the threshold cannot be increased much further. At the same time, setting a lower threshold would classify as flocking some experimental realizations in which polar order is visually nonexistent or only very short-ranged.

5. Simulation scheme

We implement Brownian dynamics simulations of Eq. (3) with Eqs. (1) and (2). We place the particles in a square box of side L with periodic boundary conditions. We use simulation units and parameter values estimated from our experiments as indicated in Table I. We use an explicit Euler-Mayurama method for the time evolution with time step $\Delta t = 10^{-4}$, and the simulations are performed for $N_{\text{steps}} = 1.4 \times 10^6$ steps, corresponding to a simulation duration $T \approx 934$ s.

We benchmark our simulations by reproducing the results of Ref. [48] using $N = 1024$ particles with turn-toward torques (Fig. S5 [55]). For turn-away torques, we perform simulations with $N = 2500$ particles. We show nonuniform flocking states in larger systems using simulations with $N = 40\,000$ particles (Fig. S10 [55]). In this case, we use a cell-list algorithm to track particle neighbors. In our simulations, we vary the area fraction $\phi_0 = N\pi\sigma^2/(4L^2)$ and the self-propulsion speed v_0 in the ranges $\phi_0 \in [0.02, 1.30]$ and $v_0 \in [0, 60]$ μm/s.

6. Quantification of hexatic order

To quantify hexatic order [60], we measure the local hexatic order of particle i defined as $\psi_{6,i} = (1/N_{\text{nn}}^i) \sum_{j=1}^{N_{\text{nn}}^i} e^{6i\theta_{ij}}$, where θ_{ij} is the angle of the segment connecting particles i and j with respect to the $\hat{\boldsymbol{x}}$ axis and N_{nn}^i is the number of nearest neighbors of particle i found through Voronoi tessellation. From it, we obtain the global

TABLE I. Parameter estimates. Parameter values as obtained in Ref. [48], except switching the head and tail dipole magnitudes. We define our simulation units based on the four first entries of this table, which we use to define the scales of length, time, energy, and electric charge, respectively.

Description and symbol	Estimate	Value in simulation units
Particle diameter $\sigma = 2R$	3 μm	1
Rotational diffusion coefficient D_r	0.15 s^{-1}	1
Thermal energy k_BT	4.11×10^{-21} J	1
Dielectric permittivity of the solvent ϵ	6.95×10^{-10} $C^2/(N\,m^2)$	1
Translational diffusion coefficient D_t	0.16 $\mu m^2/s$	0.11
Translational drag coefficient ξ_t	25 mPa s μm	9
Rotational drag coefficient ξ_r	75 mPa s μm^3	3
Electrostatic screening length λ	120 μm	40
Dipole shift distance ℓ	0.56 μm	0.19
Electric field amplitude E_0	83 V/mm	179
Head dipole magnitude $\lvert d_h\rvert$	9.76×10^{-22} C m	112
Tail dipole magnitude $\lvert d_t\rvert$	4.64×10^{-22} C m	53

hexatic order $\psi_6 = (1/N)|\sum_{i=1}^{N}\psi_{6,i}|$, which is a scalar order parameter that we show in Fig. 3(a). We also obtain the hexatic angle α_i of each particle, which we show to visualize ordered domains in Figs. 3(b)–3(e). This angle indicates the projection of the local hexatic order $\psi_{6,i}$ onto its average $\Psi_6 = (1/N)\sum_{i=1}^{N}\psi_{6,i}$, obtained from the scalar product of these two complex numbers: $\psi_{6,i}\Psi_6 = |\psi_{6,i}||\Psi_6|\cos\alpha_i$.

7. Pair distribution function

To numerically obtain the pair distribution function $g(r,\varphi,\theta)$, we build a histogram of the number of particles $N_l(r,\varphi,\theta)$ at distance r, positional angle ϕ, and relative orientation θ [Fig. 4(a)]. We normalize the count to obtain $g(r,\varphi,\theta) = 2\pi N_l(r,\varphi,\theta)/[A(r)Nt_{\mathrm{run}}\rho\Delta\theta]$, where $A(r) = r\Delta r\Delta\varphi$ is the area of the annular segment of radial width Δr and angular width $\Delta\varphi$, ρ is the number density, t_{run} is the number of snapshots, and $\Delta\theta$ is the size of the relative-orientation bins [78]. The histogram is built over 1000 independent realizations, with a total of 93289 snapshots. We choose bins of $\pi/180$ for φ, 0.1 for r, and $\pi/2$ for θ, as shown in Figs. 4(b)–4(e).

8. Scattering simulations

We initialize binary scattering events by placing the two particles at a distance $|\boldsymbol{r}_{12}| = r_{\mathrm{int}}$, when they enter the interaction range [Figs. 5(a) and 5(b)]. We choose the axes so that the two particles are initially separated along the $\hat{\boldsymbol{y}}$ axis [Fig. S12(a) [55]]. The direction of the interparticle distance vector, in general, varies throughout the scattering event [Fig. S12(a) [55]]. For convenience, in these simulations we describe the particle orientations via the angles θ_1 and θ_2 measured with respect to the axis perpendicular to the interparticle distance vector [Fig. S12(a) [55]]. Based on these angles, the initial configuration is characterized by the incoming half-angle $\bar{\theta} = \arg(e^{i\theta_1} + e^{i\theta_2})$ and the angle difference $\theta = \theta_2 - \theta_1$ [Fig. S12(b) [55]].

To simulate binary scattering events, we rewrite Eq. (3) without noise in terms of the angles θ_1 and θ_2 and the interparticle distance $r = |\boldsymbol{r}_{12}|$ as

$$\dot{r} = \frac{C}{r^4}e^{-r/\lambda} - v_0(\sin\theta_1 - \sin\theta_2), \tag{A1a}$$

$$\dot{\theta}_1 = -\frac{1}{r^4}e^{-r/\lambda}\cos\theta_1 - \frac{v_0}{r}(\cos\theta_1 - \cos\theta_2), \tag{A1b}$$

$$\dot{\theta}_2 = \frac{1}{r^4}e^{-r/\lambda}\cos\theta_2 - \frac{v_0}{r}(\cos\theta_1 - \cos\theta_2), \tag{A1c}$$

where C is a parameter that captures the repulsion strength in Eq. (1) relative to that of torques in Eq. (2). The second term in Eqs. (A1b) and (A1c) is the geometric contribution that accounts for the variation of the interparticle distance vector $\boldsymbol{r}_{12}$ as particles move.

We then sample the initial angles $\theta_1(t=0)$ and $\theta_2(t=0)$ from the interval $[-\pi,\pi]$ in steps of $2\pi/100$. For each scattering configuration, we numerically evolve the distance and orientations of the particles according to Eq. (A1) until the distance r reaches r_{int} again and the particles point away from each other, so that they leave the interaction range. For each of these evolutions, we measure the momentum change $\delta\boldsymbol{p} = \hat{\boldsymbol{n}}_1' + \hat{\boldsymbol{n}}_2' - \hat{\boldsymbol{n}}_1 - \hat{\boldsymbol{n}}_2$, where primes indicate the final state, and we use it to numerically perform the integral in Eq. (7) to obtain the average forward momentum change $\langle\boldsymbol{p}\cdot\delta\boldsymbol{p}\rangle_{\bar{\theta},\theta}$.

From this quantity, we calculate the growth rate of the polarity, given by $a = \langle\boldsymbol{p}\cdot\delta\boldsymbol{p}\rangle_{\bar{\theta},\theta} - D_r$. When $a < 0$, the isotropic state is linearly stable, and the polarity vanishes, $P = 0$. When $a > 0$, the isotropic state is linearly unstable, and it gives rise to flocking. To calculate the steady-state polarity of the flocking state, shown in Fig. 5(d), we expand the polarity equation to third order as

$$\partial_t P = aP - bP^3, \tag{A2}$$

and we calculate the prefactor of the third-order term, which is given by [64]

$$b = \langle(1/2 - \cos\theta)\boldsymbol{p}\cdot\delta\boldsymbol{p}\rangle_{\bar{\theta},\theta}. \tag{A3}$$

We obtain $b > 0$. Therefore, in the range of parameters that we explore, the system undergoes a second-order transition [64]. Finally, we obtain the steady-state polarity as

$$P = \sqrt{a/b}. \tag{A4}$$

To show that repulsion is required for flocking via turn-away interactions, we vary the repulsion strength C in Eq. (A1a) from 0 up to the value obtained from the experimental estimates in Table I. We then calculate $\langle\boldsymbol{p}\cdot\delta\boldsymbol{p}\rangle_{\bar{\theta},\theta}$ for each value of C [Fig. 5(c)].

APPENDIX B: COARSE-GRAINING: FROM THE MICROSCOPIC MODEL TO A HYDRODYNAMIC DESCRIPTION

Here, we provide a systematic coarse-graining of the microscopic equations of motion [Eq. (3)] to derive the growth rate of the polarity field $\boldsymbol{P}$ [Eqs. (4)–(6)], which determines the onset of flocking. To this end, we combine and adapt the derivations in Refs. [23,48].

We start with the Smoluchowski equation, which governs the evolution of the full N-particle distribution function of the system $\Psi_N(\boldsymbol{r}_1,\hat{\boldsymbol{n}}_1,\ldots,\boldsymbol{r}_N,\hat{\boldsymbol{n}}_N;t)$. We then break it into the BBGKY hierarchy of equations for the $1,2,3,\ldots$-particle distribution functions. We truncate the hierarchy at the two-particle order, with pair correlations encoded in integrals known as the collective force and torque. We then perform a gradient expansion of these

integrals, which thereby become local terms in the hydrodynamic equations. Finally, we obtain the hydrodynamic equations by defining continuum fields like the density and the polarity fields as moments of the one-particle distribution function $\Psi_1(\boldsymbol{r}_1, \hat{\boldsymbol{n}}_1; t)$.

1. Smoluchowski equation and the BBGKY hierarchy

The behavior of the system encoded in the set of coupled Langevin equations Eq. (3) can be equivalently described by the Smoluchowski equation for the N-particle distribution function $\Psi_N(\boldsymbol{r}_1, \hat{\boldsymbol{n}}_1, \ldots, \boldsymbol{r}_N, \hat{\boldsymbol{n}}_N; t)$, which is the probability density of finding the N particles at positions $\boldsymbol{r}_1, \ldots, \boldsymbol{r}_N$ with orientations $\hat{\boldsymbol{n}}_1, \ldots, \hat{\boldsymbol{n}}_N$ at time t:

$$\partial_t \Psi_N = -\sum_{i=1}^{N} [\boldsymbol{\nabla}_i \cdot \boldsymbol{J}_{t,i} + \hat{\boldsymbol{n}}_i \times \partial_{\hat{\boldsymbol{n}}_i} \cdot \boldsymbol{J}_{r,i}]. \tag{B1}$$

Here, $\hat{\boldsymbol{n}} \times \partial_{\hat{\boldsymbol{n}}}$ is the rotation operator, and $\boldsymbol{J}_t$ and $\boldsymbol{J}_r$ are the translational and rotational probability currents, respectively, given by

$$\boldsymbol{J}_{t,i} = \left[v_0 \hat{\boldsymbol{n}}_i + \frac{\boldsymbol{F}_i}{\xi_t} \right] \Psi_N - D_t \boldsymbol{\nabla}_i \Psi_N, \tag{B2a}$$

$$\boldsymbol{J}_{r,i} = \frac{\boldsymbol{\Gamma}_i}{\xi_r} \Psi_N - D_r \hat{\boldsymbol{n}}_i \times \partial_{\hat{\boldsymbol{n}}_i} \Psi_N. \tag{B2b}$$

Hereafter, we describe the two-dimensional particle orientation $\hat{\boldsymbol{n}}_i$ in terms of the angle θ_i: $\hat{\boldsymbol{n}}_i = (\cos\theta_i, \sin\theta_i)^T$.

Integrating over the positions and orientations of all particles but one, we obtain an equation for the one-particle distribution function $\Psi_1(\boldsymbol{r}_1, \theta_1; t)$:

$$\begin{aligned} \partial_t \Psi_1 = &-\boldsymbol{\nabla}_1 \cdot [(v_0 \hat{\boldsymbol{n}}_1 - D_t \boldsymbol{\nabla}_1) \Psi_1] - \boldsymbol{\nabla}_1 \cdot \frac{\boldsymbol{F}_{\text{int}}}{\xi_t} \\ &- \partial_{\theta_1} \frac{\hat{\boldsymbol{z}} \cdot \boldsymbol{\Gamma}_{\text{int}}}{\xi_r} + D_r \partial_{\theta_1}^2 \Psi_1. \end{aligned} \tag{B3}$$

Here, $\boldsymbol{F}_{\text{int}}$ and $\boldsymbol{\Gamma}_{\text{int}}$ are the collective force and torque, respectively, which encode the effects of interactions on particle 1. For pairwise interactions, the collective force and torque can be expressed in terms of the two-particle distribution function $\Psi_2(\boldsymbol{r}_1, \theta_1, \boldsymbol{r}_2, \theta_2; t)$ as

$$\begin{aligned} &\boldsymbol{F}_{\text{int}}(\boldsymbol{r}_1, \theta_1; t) \\ &\quad = -\int d^2\boldsymbol{r}' d\theta' F(|\boldsymbol{r}' - \boldsymbol{r}_1|) \frac{\boldsymbol{r}' - \boldsymbol{r}_1}{|\boldsymbol{r}' - \boldsymbol{r}_1|} \Psi_2(\boldsymbol{r}_1, \theta_1, \boldsymbol{r}', \theta'; t), \end{aligned} \tag{B4a}$$

$$\begin{aligned} &\boldsymbol{\Gamma}_{\text{int}}(\boldsymbol{r}_1, \theta_1; t) \\ &\quad = \int d^2\boldsymbol{r}' d\theta' \Gamma(|\boldsymbol{r}' - \boldsymbol{r}_1|) \hat{\boldsymbol{n}}_1 \times \frac{\boldsymbol{r}' - \boldsymbol{r}_1}{|\boldsymbol{r}' - \boldsymbol{r}_1|} \Psi_2(\boldsymbol{r}_1, \theta_1, \boldsymbol{r}', \theta'; t). \end{aligned} \tag{B4b}$$

Here,

$$F(r) = \frac{3(d_h + d_t)^2}{4\pi\epsilon} \frac{e^{-r/\lambda}}{r^4}, \tag{B5a}$$

$$\Gamma(r) = \frac{3\ell(d_h^2 - d_t^2)}{4\pi\epsilon} \frac{e^{-r/\lambda}}{r^4} \tag{B5b}$$

are the scalar magnitudes of the interaction force and torque in Eqs. (1) and (2).

With the collective force and torque given by Eq. (B4), Eq. (B3) is an integro-differential equation for Ψ_1 that involves Ψ_2. Therefore, Eq. (B3) is the first equation in the BBGKY hierarchy. To truncate the hierarchy, we decompose Ψ_2 as

$$\Psi_2(\boldsymbol{r}_1, \theta_1, \boldsymbol{r}', \theta'; t) = \Psi_1(\boldsymbol{r}', \theta'; t) g(\boldsymbol{r}', \theta' | \boldsymbol{r}_1, \theta_1; t) \Psi_1(\boldsymbol{r}_1, \theta_1; t). \tag{B6}$$

Here, $\Psi_2(\boldsymbol{r}_1, \theta_1, \boldsymbol{r}', \theta'; t)$ is the density of particle pairs with one particle at position $\boldsymbol{r}_1$ with orientation θ_1 and another particle at position $\boldsymbol{r}'$ with orientation θ' at time t. Respectively, g is the dimensionless pair distribution function that encodes the conditional probability of finding a particle at position $\boldsymbol{r}'$ and orientation θ' given that another particle is at position $\boldsymbol{r}_1$ with orientation θ_1. Introducing this decomposition into Eq. (B3) allows us to express it as a closed equation for Ψ_1, hence closing the hierarchy. This closure goes beyond the molecular chaos approximation, as it keeps information about pair correlations in the pair distribution function g.

In homogeneous steady states, the probability distributions are time independent, and the pair correlations do not depend on the coordinates of a given particle but only on the relative coordinates of particle pairs. Hence, we express g in terms of the distance $|\boldsymbol{r}' - \boldsymbol{r}_1|$ between particles, the angle φ formed between the interparticle distance vector $\boldsymbol{r}' - \boldsymbol{r}_1$ and the orientation vector $\hat{\boldsymbol{n}}_1$ of particle 1, defined by $\hat{\boldsymbol{n}}_1 \cdot (\boldsymbol{r}' - \boldsymbol{r}_1) = |\boldsymbol{r}' - \boldsymbol{r}_1| \cos\varphi$, and the relative orientation $\theta' - \theta_1$. Therefore, in homogeneous steady states like the isotropic state of the Janus particle system that we analyze, we have

$$g(\boldsymbol{r}', \theta' | \boldsymbol{r}_1, \theta_1; t) = g(|\boldsymbol{r}' - \boldsymbol{r}_1|, \varphi, \theta' - \theta_1). \tag{B7}$$

With this decomposition, the collective force and torque [Eq. (B4)] are expressed, respectively, as

$$\begin{aligned} \boldsymbol{F}_{\text{int}}(\boldsymbol{r}_1, \theta_1) = &-\Psi_1(\boldsymbol{r}_1, \theta_1) \int d^2\boldsymbol{r}' d\theta' F(|\boldsymbol{r}' - \boldsymbol{r}_1|) \\ &\times \frac{\boldsymbol{r}' - \boldsymbol{r}_1}{|\boldsymbol{r}' - \boldsymbol{r}_1|} \Psi_1(\boldsymbol{r}', \theta') g(|\boldsymbol{r}' - \boldsymbol{r}_1|, \varphi, \theta' - \theta_1), \end{aligned} \tag{B8a}$$

$$\boldsymbol{\Gamma}_{\rm int}(\boldsymbol{r}_1,\theta_1)=\Psi_1(\boldsymbol{r}_1,\theta_1)\int d^2\boldsymbol{r}'d\theta'\Gamma(|\boldsymbol{r}'-\boldsymbol{r}_1|)\hat{\boldsymbol{n}}_1 \times\frac{\boldsymbol{r}'-\boldsymbol{r}_1}{|\boldsymbol{r}'-\boldsymbol{r}_1|}\Psi_1(\boldsymbol{r}',\theta')g(|\boldsymbol{r}'-\boldsymbol{r}_1|,\varphi,\theta'-\theta_1). \tag{B8b}$$

2. Gradient expansion

The collective force and torque in Eq. (B8) depend nonlocally on the one-particle distribution function $\Psi_1(\boldsymbol{r}',\theta')$. To derive local hydrodynamic equations, we perform a gradient expansion around $\boldsymbol{r}_1$:

$$\Psi_1(\boldsymbol{r}',\theta')\approx\Psi_1(\boldsymbol{r}_1,\theta')+\boldsymbol{\nabla}_{\boldsymbol{r}'}\Psi_1(\boldsymbol{r}_1,\theta')\cdot(\boldsymbol{r}'-\boldsymbol{r}_1). \tag{B9}$$

We also expand in angular Fourier modes:

$$\Psi_1(\boldsymbol{r}',\theta')=\frac{1}{2\pi}\sum_{k=0}^{\infty}e^{-ik\theta'}\tilde{\Psi}_{1,k}(\boldsymbol{r}'). \tag{B10}$$

Thus, to lowest order in the gradient expansion, we have

$$\Psi_1(\boldsymbol{r}',\theta')\approx\frac{1}{2\pi}\sum_{k=0}^{\infty}e^{-ik\theta'}\tilde{\Psi}_{1,k}(\boldsymbol{r}_1). \tag{B11}$$

Introducing Eq. (B11) into Eq. (B8b) and changing the integration variables to the relative coordinates $\boldsymbol{r}\equiv\boldsymbol{r}'-\boldsymbol{r}_1$, with polar coordinates (r,φ), and $\theta\equiv\theta'-\theta_1$, we obtain the lowest-order contribution to the collective torque:

$$\begin{aligned}\boldsymbol{\Gamma}^{(0)}_{\rm int}(\boldsymbol{r}_1,\theta_1)&=\Psi_1(\boldsymbol{r}_1,\theta_1)\int_0^{\infty}drr\Gamma(r)\int_0^{2\pi}d\varphi\sin\varphi\hat{\boldsymbol{z}}\\&\quad\times\int d\theta g(r,\varphi,\theta)\frac{1}{2\pi}\sum_{k=0}^{\infty}e^{-ik(\theta+\theta_1)}\tilde{\Psi}_{1,k}(\boldsymbol{r}_1)\\&=\Psi_1(\boldsymbol{r}_1,\theta_1)\frac{1}{2\pi}\sum_{k=0}^{\infty}e^{-ik\theta_1}\int_0^{\infty}drr\Gamma(r)\\&\quad\times\int_0^{2\pi}d\varphi\sin\varphi\hat{\boldsymbol{z}}\int d\theta g(r,\varphi,\theta)e^{-ik\theta}\tilde{\Psi}_{1,k}(\boldsymbol{r}_1).\end{aligned} \tag{B12}$$

Here, we use that $\hat{\boldsymbol{n}}_1\times\hat{\boldsymbol{r}}=\sin\varphi\hat{\boldsymbol{z}}$. Gathering all the integrals into a coefficient, we rewrite the collective torque as

$$\boldsymbol{\Gamma}^{(0)}_{\rm int}(\boldsymbol{r}_1,\theta_1)=\Psi_1(\boldsymbol{r}_1,\theta_1)\frac{1}{2\pi}\sum_{k=0}^{\infty}e^{-ik\theta_1}\tilde{\Psi}_{1,k}(\boldsymbol{r}_1)\tau_{0,k}\hat{\boldsymbol{z}}, \tag{B13}$$

where we define the coefficient

$$\tau_{0,k}=\int_0^{\infty}drr\Gamma(r)\int_0^{2\pi}d\varphi\sin\varphi\int_0^{2\pi}d\theta g(r,\varphi,\theta)e^{-ik\theta}. \tag{B14}$$

As shown in Figs. 4(b)–4(e), the pair distribution g is invariant upon simultaneous inversion of the angles φ and θ: $g(r,\varphi,\theta)=g(r,-\varphi,-\theta)$. This symmetry implies that the real part of Eq. (B14) vanishes, and, hence, only the imaginary part survives:

$$\tau_{0,k}=-i\int_0^{\infty}drr\Gamma(r)\int_0^{2\pi}d\varphi\sin\varphi\times\int_0^{2\pi}d\theta g(r,\varphi,\theta)\sin(k\theta). \tag{B15}$$

To complete the gradient expansion, we express Eq. (B3) only to lowest order in gradients:

$$\partial_t\Psi_1=-\partial_\theta\frac{\hat{\boldsymbol{z}}\cdot\boldsymbol{\Gamma}^{(0)}_{\rm int}}{\xi_r}+D_r\partial_\theta^2\Psi_1+\mathcal{O}(\boldsymbol{\nabla}). \tag{B16}$$

Here, for simplicity, we drop the subindex that was labeling particle number 1. We do this hereafter.

3. Hydrodynamic fields and polarity growth rate

The results obtained above allow us to calculate the growth rate a of the polarity field $\boldsymbol{P}$, namely, the coefficient of the lowest-order term in the hydrodynamic equation for $\boldsymbol{P}$ [Eq. (4)]. To this end, we define the hydrodynamic fields, which are the angular moments of the one-particle distribution Ψ_1. The two lowest-order moments correspond to the density and the polarity fields:

$$\rho(\boldsymbol{r},t)=\int\Psi_1(\boldsymbol{r},\theta,t)d\theta, \tag{B17a}$$

$$\boldsymbol{P}(\boldsymbol{r},t)=\int\hat{\boldsymbol{n}}(\theta)\Psi_1(\boldsymbol{r},\theta,t)d\theta. \tag{B17b}$$

In two dimensions, given that $\hat{\boldsymbol{n}}(\theta)=(\cos\theta,\sin\theta)^T$, these fields can be expressed in terms of the angular Fourier components of Ψ_1. Based on the Fourier expansion in Eq. (B10), the components are given by

$$\tilde{\Psi}_{1,k}(\boldsymbol{r},t)=\int_0^{2\pi}d\theta e^{ik\theta}\Psi_1(\boldsymbol{r},\theta,t). \tag{B18}$$

Thus, the density and polarity fields are given by the zeroth and first components as, respectively,

$$\rho(\boldsymbol{r},t)=\tilde{\Psi}_{1,0}(\boldsymbol{r},t), \tag{B19a}$$

$$\boldsymbol{P}(\boldsymbol{r},t)=\begin{pmatrix}\mathrm{Re}\,\tilde{\Psi}_{1,1}(\boldsymbol{r},t)\\ \mathrm{Im}\,\tilde{\Psi}_{1,1}(\boldsymbol{r},t)\end{pmatrix}. \tag{B19b}$$

To obtain an equation for the angular Fourier moments $\Psi_{1,k}(\boldsymbol{r},t)$, we project Eq. (B16) according to the integral in Eq. (B18). Using integration by parts, we obtain

$$\partial_t\tilde{\Psi}_{1,k}=\frac{ik}{2\pi\xi_r}\sum_{m=0}^{\infty}\tilde{\Psi}_{1,m}\tau_{0,m}\tilde{\Psi}_{1,k-m}-D_rk^2\tilde{\Psi}_{1,k}, \tag{B20}$$

where we use Eq. (B13) and with $\tau_{0,m}$ given in Eq. (B15). The equation for the polarity field $\boldsymbol{P}$ then follows from the $k=1$ component. Among the terms in the sum over m, we keep only the lowest-order terms $m=0$ and $m=1$. Given that $\tau_{0,0}=0$, we arrive at

$$\partial_t\tilde{\Psi}_{1,1}=\frac{i}{2\pi\xi_r}\tilde{\Psi}_{1,1}\tau_{0,1}\tilde{\Psi}_{1,0}-D_r\tilde{\Psi}_{1,1}. \tag{B21}$$

Hence, using Eq. (B19), the equation for the polarity reads

$$\partial_t\boldsymbol{P}=\frac{\rho}{2\pi\xi_r}\tau_0\boldsymbol{P}-D_r\boldsymbol{P}+\mathcal{O}(\boldsymbol{\nabla}), \tag{B22}$$

where we define $\tau_0\equiv i\tau_{0,1}$, whose explicit expression is given in Eq. (6). Comparing to Eq. (4), this result provides the growth rate of the polarity field, which is given by Eq. (5) as a functional of the density field ρ.

APPENDIX C: BOLTZMANN KINETIC THEORY

In this section, we provide details of the Boltzmann kinetic theory that we use to predict the onset of flocking from binary scattering events (Fig. 5). We follow Ref. [64], and we summarize the key steps of the derivation here for reference. We start from the Boltzmann equation for the evolution of the one-particle orientation distribution $f(\theta_1,t)$, where θ_1 is the particle orientation angle. This distribution relates to the full one-particle distribution $\Psi_1(\boldsymbol{r}_1,\theta_1,t)$ in Appendix B as $f(\theta_1,t)=\int d^2\boldsymbol{r}_1\Psi_1(\boldsymbol{r}_1,\theta_1,t)$. The orientation distribution evolves as

$$\partial_t f(\theta_1,t)=I_{\mathrm{scatt}}[f,f]+I_{\mathrm{diff}}[f], \tag{C1}$$

where $I_{\mathrm{scatt}}[f,f]$ and $I_{\mathrm{diff}}[f]$ are functionals representing the changes in particle orientation due to binary scattering events and rotational diffusion, respectively.

We then use Eq. (C1) to derive the dynamics of the global polarity $\boldsymbol{P}(t)=\int\hat{\boldsymbol{n}}_1(\theta_1)f(\theta_1,t)d\theta_1$, with $\hat{\boldsymbol{n}}_1$ the particle orientation vector [64]. A scattering event changes the polarity by an amount $\delta\boldsymbol{p}$, which depends on the geometry of the scattering event parametrized by the incoming angle difference $\theta=\theta_2-\theta_1$ and half-angle $\bar{\theta}=\arg\left(e^{i\theta_1}+e^{i\theta_2}\right)$ (Fig. S12 [55]). Respectively, in a rotational diffusion event, a particle changes its orientation by a random angle η with probability $\mathcal{P}_\eta(\eta)$, which produces a polarity change $\delta\boldsymbol{p}_{\mathrm{diff}}(\theta_1,\eta)=\mathcal{R}_\eta\hat{\boldsymbol{n}}_1(\theta_1)-\hat{\boldsymbol{n}}_1(\theta_1)$, with $\mathcal{R}_\eta$ being the corresponding rotation matrix. Then, the equation for the polarity reads

$$\frac{d\boldsymbol{P}}{dt}=\gamma\Phi_f^{\mathrm{scatt}}[\delta\boldsymbol{p}(\bar{\theta},\theta)]+\gamma_{\mathrm{diff}}\Phi_f^{\mathrm{diff}}[\delta\boldsymbol{p}_{\mathrm{diff}}(\theta_1,\eta)], \tag{C2}$$

where γ and γ_{diff} are characteristic rates of the scattering and diffusion processes, respectively, and the corresponding functionals are given by

$$\Phi_f^{\mathrm{scatt}}[\ldots]=\int_0^{2\pi}d\bar{\theta}\int_0^{2\pi}d\theta K(\theta)f(\theta_1,t)f(\theta_2,t)(\ldots), \tag{C3a}$$

$$\Phi_f^{\mathrm{diff}}[\ldots]=\int_0^{2\pi}d\theta_1\int d\eta\mathcal{P}_\eta(\eta)f(\theta_1,t)(\ldots). \tag{C3b}$$

Here, we take the molecular chaos hypothesis, which assumes that the distributions of two particles before a scattering event are independent. Hence, the two distribution functions f in the scattering functional factorized as seen in Eq. (C3a). The additional factor $K(\theta)$ in Eq. (C3a) is the form factor of a scattering event with angle difference θ. For particles that undergo scattering events at a fixed impact parameter, like in our case, the form factor is $K(\theta)=|\sin(\theta/2)|$, which can be obtained from the Boltzmann cylinder construction [64,79].

To obtain an equation for the polar order $P=|\boldsymbol{P}|$, we project Eq. (C2) along the polarity direction $\hat{\boldsymbol{P}}$, which yields [64]

$$\frac{dP}{dt}=\rho v_0r_{\mathrm{int}}\Phi_f^{\mathrm{scatt}}[(\hat{\boldsymbol{p}}\cdot\delta\boldsymbol{p})\cos\bar{\theta}]-D_rP. \tag{C4}$$

Here, we use that the characteristic scattering rate γ in Eq. (C2) is given by $\gamma=\rho v_0r_{\mathrm{int}}$ for a gas of self-propelled particles with speed v_0, concentration ρ, and interaction range r_{int}, which acts as the impact parameter [see Appendix A and Fig. S12(a) [55]]. The second term in Eq. (C4) is obtained by explicit integration of the diffusion functional. It describes the loss of polar order, with a coefficient that we identify with the rotational diffusivity D_r of the particles. The explicit integration gives D_r in terms of the rate γ_{diff} in Eq. (C2) and the angular noise distribution $\mathcal{P}_\eta(\eta)$:

$$D_r=\gamma_{\mathrm{diff}}\left(1-\int d\eta\mathcal{P}_\eta(\eta)\cos\eta\right). \tag{C5}$$

To evaluate the scattering functional, we need to know the orientation distribution $f(\theta_1,t)$. To this end, we take an ansatz of the form $f(\theta_1,t)=f_{P(t)}(\theta_1)$, and we assume that the distribution of orientations in the isotropic phase is uniform up to the constraint

$$\left|\int_0^{2\pi}\hat{\boldsymbol{n}}_1(\theta_1)f_P(\theta_1)d\theta_1\right|=P. \tag{C6}$$

The distribution that satisfies these conditions is known as the von Mises distribution, and it is given by [64]

$$f_P(\theta_1) = \frac{e^{\kappa(\theta_1)\cos\theta_1}}{2\pi I_0[\kappa(P)]}, \tag{C7}$$

with $\kappa(P)$ determined from

$$\frac{I_1[\kappa(P)]}{I_0[\kappa(P)]} = P, \tag{C8}$$

where I_n are the modified Bessel functions of the first kind and of order n.

We then use this distribution in the scattering functional in Eq. (C4) and expand around the isotropic state to derive the equation for the polar order to linear order. The von Mises distribution expands into

$$f_P(\theta_1) \approx \frac{1}{2\pi}(1 + 2P\cos\theta_1). \tag{C9}$$

Introducing all the results above into Eq. (C4), we obtain

$$\frac{dP}{dt} \approx aP, \tag{C10}$$

with

$$\begin{aligned} a &= \frac{\rho v_0 r_{\mathrm{int}}}{(2\pi)^2}\int_0^{2\pi} d\bar{\theta}\int_0^{2\pi} d\theta |\sin(\theta/2)|\boldsymbol{p}\cdot\delta\boldsymbol{p}(\bar{\theta},\theta) - D_r \\ &= \frac{\rho v_0 r_{\mathrm{int}}}{2\pi}\int_{-\pi}^{\pi} d\theta |\sin(\theta/2)|\langle\boldsymbol{p}\cdot\delta\boldsymbol{p}(\bar{\theta},\theta)\rangle_{\bar{\theta}} - D_r. \end{aligned} \tag{C11}$$

The first term is the change in polar order due to scattering events as provided in Eq. (7) in the main text.

[1] Tamás Vicsek and Anna Zafeiris, *Collective motion*, Phys. Rep. **517**, 71 (2012).

[2] Andrea Cavagna and Irene Giardina, *Bird flocks as condensed matter*, Annu. Rev. Condens. Matter Phys. **5**, 183 (2014).

[3] Fernando Peruani, Jörn Starruß, Vladimir Jakovljevic, Lotte Søgaard-Andersen, Andreas Deutsch, and Markus Bär, *Collective motion and nonequilibrium cluster formation in colonies of gliding bacteria*, Phys. Rev. Lett. **108**, 098102 (2012).

[4] Volker Schaller, Christoph Weber, Christine Semmrich, Erwin Frey, and Andreas R. Bausch, *Polar patterns of driven filaments*, Nature (London) **467**, 73 (2010).

[5] Tamás Vicsek, András Czirók, Eshel Ben-Jacob, Inon Cohen, and Ofer Shochet, *Novel type of phase transition in a system of self-driven particles*, Phys. Rev. Lett. **75**, 1226 (1995).

[6] John Toner and Yuhai Tu, *Long-range order in a two-dimensional dynamical XY model: How birds fly together*, Phys. Rev. Lett. **75**, 4326 (1995).

[7] Antoine Bricard, Jean-Baptiste Caussin, Nicolas Desreumaux, Olivier Dauchot, and Denis Bartolo, *Emergence of macroscopic directed motion in populations of motile colloids*, Nature (London) **503**, 95 (2013).

[8] Andreas Kaiser, Alexey Snezhko, and Igor S. Aranson, *Flocking ferromagnetic colloids*, Sci. Adv. **3**, e1601469 (2017).

[9] Delphine Geyer, Alexandre Morin, and Denis Bartolo, *Sounds and hydrodynamics of polar active fluids*, Nat. Mater. **17**, 789 (2018).

[10] M. Reza Shaebani, Adam Wysocki, Roland G. Winkler, Gerhard Gompper, and Heiko Rieger, *Computational models for active matter*, Nat. Rev. Phys. **2**, 181 (2020).

[11] Markus Bär, Robert Großmann, Sebastian Heidenreich, and Fernando Peruani, *Self-propelled rods: Insights and perspectives for active matter*, Annu. Rev. Condens. Matter Phys. **11**, 441 (2020).

[12] Hugues Chaté, *Dry aligning dilute active matter*, Annu. Rev. Condens. Matter Phys. **11**, 189 (2020).

[13] P. Baconnier, O. Dauchot, V. Démery, G. Düring, S. Henkes, C. Huepe, and A. Shee, *Self-aligning polar active matter*, arXiv:2403.10151v1.

[14] B. Szabó, G. J. Szöllösi, B. Gönci, Zs. Jurányi, D. Selmeczi, and Tamás Vicsek, *Phase transition in the collective migration of tissue cells: Experiment and model*, Phys. Rev. E **74**, 061908 (2006).

[15] Eliseo Ferrante, Ali Emre Turgut, Marco Dorigo, and Cristián Huepe, *Elasticity-based mechanism for the collective motion of self-propelled particles with springlike interactions: A model system for natural and artificial swarms*, Phys. Rev. Lett. **111**, 268302 (2013).

[16] D. Grossman, I. S. Aranson, and E. Ben Jacob, *Emergence of agent swarm migration and vortex formation through inelastic collisions*, New J. Phys. **10**, 023036 (2008).

[17] Julien Deseigne, Olivier Dauchot, and Hugues Chaté, *Collective motion of vibrated polar disks*, Phys. Rev. Lett. **105**, 098001 (2010).

[18] Pawel Romanczuk, I. D. Couzin, and Lutz Schimansky-Geier, *Collective motion due to individual escape and pursuit response*, Phys. Rev. Lett. **102**, 010602 (2009).

[19] R. Großmann, L. Schimansky-Geier, and P. Romanczuk, *Self-propelled particles with selective attraction-repulsion interaction: From microscopic dynamics to coarse-grained theories*, New J. Phys. **15**, 085014 (2013).

[20] Daniel Strömbom, *Collective motion from local attraction*, J. Theor. Biol. **283**, 145 (2011).

[21] Lucas Barberis and Fernando Peruani, *Large-scale patterns in a minimal cognitive flocking model: Incidental leaders, nematic patterns, and aggregates*, Phys. Rev. Lett. **117**, 248001 (2016).

[22] Lucas Barberis and Fernando Peruani, *Phase separation and emergence of collective motion in a one-dimensional system of active particles*, J. Chem. Phys. **150**, 144905 (2019).

[23] Robert Großmann, Igor S. Aranson, and Fernando Peruani, *A particle-field approach bridges phase separation and collective motion in active matter*, Nat. Commun. **11**, 5365 (2020).

[24] Miloš Knežević, Till Welker, and Holger Stark, *Collective motion of active particles exhibiting non-reciprocal orientational interactions*, Sci. Rep. **12**, 19437 (2022).
[25] Lu Chen, Kyle J. Welch, Premkumar Leishangthem, Dipanjan Ghosh, Bokai Zhang, Ting-Pi Sun, Josh Klukas, Zhanchun Tu, Xiang Cheng, and Xinliang Xu, *Molecular chaos in dense active systems*, arXiv:2302.10525.
[26] Mathias Casiulis and Dov Levine, *Emergent synchronization and flocking in purely repulsive self-navigating particles*, Phys. Rev. E **106**, 044611 (2022).
[27] L. Caprini and H. Löwen, *Flocking without alignment interactions in attractive active Brownian particles*, Phys. Rev. Lett. **130**, 148202 (2023).
[28] Rüdiger Kürsten, Jakob Mihatsch, and Thomas Ihle, *Flocking in binary mixtures of anti-aligning self-propelled particles*, arXiv:2304.05476.
[29] R. A. Kopp and S. H. L. Klapp, *Spontaneous velocity alignment of Brownian particles with feedback-induced propulsion*, Europhys. Lett. **143**, 17002 (2023).
[30] Yael Katz, Kolbjørn Tunstrøm, Christos C. Ioannou, Cristián Huepe, and Iain D. Couzin, *Inferring the structure and dynamics of interactions in schooling fish*, Proc. Natl. Acad. Sci. U.S.A. **108**, 18720 (2011).
[31] Jitesh Jhawar, Richard G. Morris, U. R. Amith-Kumar, M. Danny Raj, Tim Rogers, Harikrishnan Rajendran, and Vishwesha Guttal, *Noise-induced schooling of fish*, Nat. Phys. **16**, 488 (2020).
[32] Adam T. Hayes and Parsa Dormiani-Tabatabaei, *Self-organized flocking with agent failure: Off-line optimization and demonstration with real robots*, Proc. IEEE Int. Conf. Robot. Autom. **4**, 3900 (2002).
[33] Roberto Mayor and Carlos Carmona-Fontaine, *Keeping in touch with contact inhibition of locomotion*, Trends Cell Biol. **20**, 319 (2010).
[34] Brian Stramer and Roberto Mayor, *Mechanisms and in vivo functions of contact inhibition of locomotion*, Nat. Rev. Mol. Cell Biol. **18**, 43 (2017).
[35] Ricard Alert and Xavier Trepat, *Physical models of collective cell migration*, Annu. Rev. Condens. Matter Phys. **11**, 77 (2020).
[36] Bart Smeets, Ricard Alert, Jiří Pešek, Ignacio Pagonabarraga, Herman Ramon, and Romaric Vincent, *Emergent structures and dynamics of cell colonies by contact inhibition of locomotion*, Proc. Natl. Acad. Sci. U.S.A. **113**, 14621 (2016).
[37] Tetsuya Hiraiwa, *Dynamic self-organization of idealized migrating cells by contact communication*, Phys. Rev. Lett. **125**, 268104 (2020).
[38] Ravi A. Desai, Smitha B. Gopal, Sophia Chen, and Christopher S. Chen, *Contact inhibition of locomotion probabilities drive solitary versus collective cell migration*, J. R. Soc. Interface **10**, 20130717 (2013).
[39] Maureen Cetera, Guillermina R. Ramirez-San Juan, Patrick W. Oakes, Lindsay Lewellyn, Michael J. Fairchild, Guy Tanentzapf, Margaret L. Gardel, and Sally Horne-Badovinac, *Epithelial rotation promotes the global alignment of contractile actin bundles during Drosophila egg chamber elongation*, Nat. Commun. **5**, 5511 (2014).
[40] Chiara Malinverno *et al.*, *Endocytic reawakening of motility in jammed epithelia*, Nat. Mater. **16**, 587 (2017).
[41] Shreyansh Jain, Victoire M. L. Cachoux, Gautham H. N. S. Narayana, Simon de Beco, Joseph D'Alessandro, Victor Cellerin, Tianchi Chen, Mélina L. Heuzé, Philippe Marcq, René-Marc Mège, Alexandre J. Kabla, Chwee Teck Lim, and Benoit Ladoux, *The role of single-cell mechanical behaviour and polarity in driving collective cell migration*, Nat. Phys. **16**, 802 (2020).
[42] Tom Brandstätter, David B. Brückner, Yu Long Han, Ricard Alert, Ming Guo, and Chase P. Broedersz, *Curvature induces active velocity waves in rotating spherical tissues*, Nat. Commun. **14**, 1643 (2023).
[43] Emma Lång, Anna Lång, Pernille Blicher, Torbjørn Rognes, Paul Gunnar Dommersnes, and Stig Ove Bøe, *Topology-guided polar ordering of collective cell migration*, Sci. Adv. **10**, eadk4825 (2024).
[44] Tzer Han Tan, Aboutaleb Amiri, Irene Seijo-Barandiarán, Michael F. Staddon, Anne Materne, Sandra Tomas, Charlie Duclut, Marko Popović, Anne Grapin-Botton, and Frank Jülicher, *Emergent chirality in active solid rotation of pancreas spheres*, 10.1101/2022.09.29.510101.
[45] M. C. Marchetti, J. F. Joanny, S. Ramaswamy, T. B. Liverpool, J. Prost, Madan Rao, and R. A. Simha, *Hydrodynamics of soft active matter*, Rev. Mod. Phys. **85**, 1143 (2013).
[46] Michael E. Cates and Julien Tailleur, *Motility-induced phase separation*, Annu. Rev. Condens. Matter Phys. **6**, 219 (2015).
[47] L. Huber, R. Suzuki, T. Krüger, E. Frey, and A. R. Bausch, *Emergence of coexisting ordered states in active matter systems*, Science **361**, 255 (2018).
[48] Jie Zhang, Ricard Alert, Jing Yan, Ned S. Wingreen, and Steve Granick, *Active phase separation by turning towards regions of higher density*, Nat. Phys. **17**, 961 (2021).
[49] Jing Yan, Ming Han, Jie Zhang, Cong Xu, Erik Luijten, and Steve Granick, *Reconfiguring active particles by electrostatic imbalance*, Nat. Mater. **15**, 1095 (2016).
[50] Marjolein N. van der Linden, Lachlan C. Alexander, Dirk G. A. L. Aarts, and Olivier Dauchot, *Interrupted motility induced phase separation in aligning active colloids*, Phys. Rev. Lett. **123**, 098001 (2019).
[51] Junichiro Iwasawa, Daiki Nishiguchi, and Masaki Sano, *Algebraic correlations and anomalous fluctuations in ordered flocks of Janus particles fueled by an ac electric field*, Phys. Rev. Res. **3**, 043104 (2021).
[52] Sumit Gangwal, Olivier J. Cayre, Martin Z. Bazant, and Orlin D. Velev, *Induced-charge electrophoresis of metallodielectric particles*, Phys. Rev. Lett. **100**, 058302 (2008).
[53] Jeffrey L. Moran and Jonathan D. Posner, *Phoretic self-propulsion*, Annu. Rev. Fluid Mech. **49**, 511 (2017).
[54] Kyle J. M. Bishop, Sibani Lisa Biswal, and Bhuvnesh Bharti, *Active colloids as models, materials, and machines*, Annu. Rev. Chem. Biomol. Eng. **14**, 1 (2023).
[55] See Supplemental Material at http://link.aps.org/supplemental/10.1103/PhysRevX.14.031008 for supplemental figures and movies.
[56] Guillaume Grégoire, Hugues Chaté, and Yuhai Tu, *Moving and staying together without a leader*, Physica (Amsterdam) **181D**, 157 (2003).
[57] Andreas M. Menzel and Hartmut Löwen, *Traveling and resting crystals in active systems*, Phys. Rev. Lett. **110**, 055702 (2013).

[58] E. Wigner, *On the interaction of electrons in metals*, Phys. Rev. **46**, 1002 (1934).
[59] Marine Le Blay and Alexandre Morin, *Repulsive torques alone trigger crystallization of constant speed active particles*, Soft Matter **18**, 3120 (2022).
[60] B. I. Halperin and D. R. Nelson, *Theory of two-dimensional melting*, Phys. Rev. Lett. **41**, 121 (1978).
[61] Berend van der Meer, Laura Filion, and Marjolein Dijkstra, *Fabricating large two-dimensional single colloidal crystals by doping with active particles*, Soft Matter **12**, 3406 (2016).
[62] Sophie Ramananarivo, Etienne Ducrot, and Jeremie Palacci, *Activity-controlled annealing of colloidal monolayers*, Nat. Commun. **10**, 3380 (2019).
[63] Elena Sesé-Sansa, Demian Levis, and Ignacio Pagonabarraga, *Microscopic field theory for structure formation in systems of self-propelled particles with generic torques*, J. Chem. Phys. **157**, 224905 (2022).
[64] Khanh-Dang Nguyen Thu Lam, Michael Schindler, and Olivier Dauchot, *Polar active liquids: A universal classification rooted in nonconservation of momentum*, J. Stat. Mech. (2015) P10017.
[65] Delphine Geyer, David Martin, Julien Tailleur, and Denis Bartolo, *Freezing a flock: Motility-induced phase separation in polar active liquids*, Phys. Rev. X **9**, 031043 (2019).
[66] Qianhong Yang, Maoqiang Jiang, Francesco Picano, and Lailai Zhu, *Shaping active matter from crystalline solids to active turbulence*, Nat. Commun. **15**, 2874 (2024).
[67] Gabriel S. Redner, Michael F. Hagan, and Aparna Baskaran, *Structure and dynamics of a phase-separating active colloidal fluid*, Phys. Rev. Lett. **110**, 055701 (2013).
[68] Jeremie Palacci, Stefano Sacanna, Asher Preska Steinberg, David J. Pine, and Paul M. Chaikin, *Living crystals of light-activated colloidal surfers*, Science **339**, 936 (2013).
[69] Ahmad K. Omar, Katherine Klymko, Trevor GrandPre, and Phillip L. Geissler, *Phase diagram of active Brownian spheres: Crystallization and the metastability of motility-induced phase separation*, Phys. Rev. Lett. **126**, 188002 (2021).
[70] Rajesh Singh and R. Adhikari, *Universal hydrodynamic mechanisms for crystallization in active colloidal suspensions*, Phys. Rev. Lett. **117**, 228002 (2016).
[71] Shashi Thutupalli, Delphine Geyer, Rajesh Singh, Ronojoy Adhikari, and Howard A. Stone, *Flow-induced phase separation of active particles is controlled by boundary conditions*, Proc. Natl. Acad. Sci. U.S.A. **115**, 5403 (2018).
[72] Ephraim S. Bililign, Florencio Balboa Usabiaga, Yehuda A. Ganan, Alexis Poncet, Vishal Soni, Sofia Magkiriadou, Michael J. Shelley, Denis Bartolo, and William T. M. Irvine, *Motile dislocations knead odd crystals into whorls*, Nat. Phys. **18**, 212 (2022).
[73] Tzer Han Tan, Alexander Mietke, Junang Li, Yuchao Chen, Hugh Higinbotham, Peter J. Foster, Shreyas Gokhale, Jörn Dunkel, and Nikta Fakhri, *Odd dynamics of living chiral crystals*, Nature (London) **607**, 287 (2022).
[74] Julian Bialké, Thomas Speck, and Hartmut Löwen, *Crystallization in a dense suspension of self-propelled particles*, Phys. Rev. Lett. **108**, 168301 (2012).
[75] Christoph A. Weber, Christopher Bock, and Erwin Frey, *Defect-mediated phase transitions in active soft matter*, Phys. Rev. Lett. **112**, 168301 (2014).
[76] G. Briand and O. Dauchot, *Crystallization of self-propelled hard discs*, Phys. Rev. Lett. **117**, 098004 (2016).
[77] Thibault Bertrand, Joseph d'Alessandro, Ananyo Maitra, Shreyansh Jain, Barbara Mercier, René-Marc Mège, Benoit Ladoux, and Raphaël Voituriez, *Clustering and ordering in cell assemblies with generic asymmetric aligning interactions*, Phys. Rev. Res. **6**, 023022 (2024).
[78] Michael P. Allen and Dominic J. Tildesley, *Computer Simulation of Liquids*, 2nd ed. (Oxford University Press, New York, 2017).
[79] Mehran Kardar, *Statistical Physics of Particles* (Cambridge University Press, Cambridge, England, 2007).